Microsc. Microanal. 14, 405–417, 2008
doi:10.1017/S1431927608080859

Microscopy AND Microanalysis

Structural, Mineralogical, and Biochemical Diversity in the Lower Part of the Pearl Layer of Cultivated Seawater Pearls from Polynesia

Jean-Pierre Cuif,[1,*] Alexander D. Ball,[2] Yannicke Dauphin,[1] Bastien Farre,[1] Julius Nouet,[1] Alberto Perez-Huerta,[3] Murielle Salomé,[4] and C. Terry Williams[2]

[1]*University Paris-Sud, Faculty of Sciences, UMR 8148 IDES, Bat 504 Geology, 91405 Orsay, France*
[2]*Natural History Museum, Department of Mineralogy, Cromwell Road, London SW7 5BD, UK*
[3]*University of Glasgow, Department of Geographical & Earth Sciences, Gregory Building, Glasgow G12 8QQ, UK*
[4]*European Synchrotron Radiation Facility, 6 rue J. Horowitz, BP 220, 38043 Grenoble, France*

Abstract: A series of Polynesian pearls has been investigated with particular attention to the structural and compositional patterns of the early developmental stages of the pearl layer. These initial steps in pearl formation bear witness of the metabolic changes that have occurred during the pearl-sac formation. The resulting structurally and biochemically complex structures have been investigated using a variety of techniques that provide us with information concerning both mineral phases and the organic components. Results are discussed with respect to our understanding of the biomineralization mechanisms, as well as for the grafting process.

Key words: pearl growth, biomineralization, nacre, prisms, calcite, aragonite, microstructure

Introduction

The pearl cultivation method initiated by Mise and Nishikawa in 1907 is still employed today. The first key stage in the process is the cutting of the "graft," which comprises a fragment of the nacreous-producing area of the animal's mantle that is a few square-millimeters wide. The graft is then inserted into another living specimen (slightly opened) together with a nucleus, which is a mineral sphere several millimeters in diameter (typically taken from an aragonitic shell). Usually, the nucleus is first placed within the internal cavity of the "receiver" specimen, in the vicinity of the gonad. The graft is then deposited onto the nucleus, taking care to position its external cell layer—i.e., the only one with mineralizing activity—against the nucleus surface. Once the nucleus and mineralizing epithelium are in close contact, the grafting operation is over and the animal is placed back into culture. By means of a process not fully understood, the mantle fragment covers the whole nucleus surface after 7 days (Gervis & Sims, 1992). Approximately 1 month after the grafting operation, a monolayer epithelium—the "pearl-sac"—is formed and newly formed materials become visible onto the nucleus. One or two years later, depending on the pearl quality expected by the producer (i.e., the thickness of the nacreous pearl layer), the pearls are harvested.

Received February 21, 2008; accepted July 16, 2008
*Corresponding author. E-mail: jean-pierre.cuif@u-psud.fr

It has long been recognized that, in contrast to a simple reappearance of the nacreous mineralization, initial structures produced by the pearl-sac after grafting operation are more complex. Kawakami (1952) hypothesized that, as a newly formed epithelium, the pearl-sac begins its mineralizing activity by developing a microstructural sequence comparable to the initial shell microstructure appearing during the postmetamorphosis stage of the young *Pinctada*. Following this view, nacreous material is produced only after deposition of a periostracum-like layer onto the nucleus, then the calcitic prisms are formed and, finally, the nacreous tablets.

Applying a range of chemical and physical techniques, we demonstrate that, far from repeating the typical microstructure of *Pinctada* shells, the layers located between the nucleus and the nacreous pearly material exhibit diverse organic and mineral structures. These complex structures bear witness to the metabolism of the pearl-sac during its early period of secretion and provide us with important information concerning this critical phase of pearl production.

Materials and Methods

Materials

Thirty pearls from various Polynesian atolls were sectioned diametrically using a 0.25-mm-thick diamond saw. The pearls were provided by the Polynesian pearl control office (Motu Uta, Papeete) and the EVAAM Research Station at

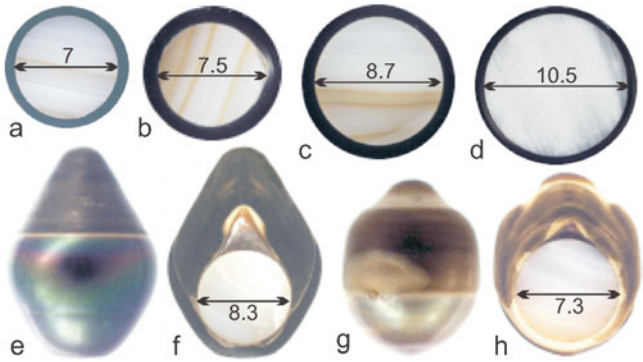

Figure 1. Some of the pearls studied. Note the variable thickness of the pearl layers (essentially dependent on the cultivation time). The two "baroque" pearls below (**e**,**g**: external views; **f**,**h**: sections) exemplify abnormal development that can occur within the pearl-sac.

Rangiroa, or by private producers (R. Wan at Marutea-Sud and T. Bernicot at Moorea). The studied pearls were mostly spherical (Fig. 1a–d), but some belong to the "baroque" pearls (i.e., with more or less irregular protuberances, e.g., Fig. 1e–g). In two of the more spectacular specimens, an abnormal growth mode is visible (Fig. 1e–h). The sections were polished using a sequence of Buehler abrasive papers, followed by diamond paste in a water suspension. Microstructural observations and chemical characterizations were focused on the basal part of the pearl layer.

Fluorescence Microscopy

A ZEISS Universal microscope was used in ultraviolet (UV) epifluorescence mode using a mercury lamp fitted with UV (365 nm) and blue (435 nm) filters.

Confocal microscopy was carried out in the Electron Microscopy and Mineral Analysis Division in the Mineralogy Department at the Natural History Museum (NHM), London, using a LEICA TCS-NT SP microscope. All the samples examined had been previously sectioned and polished to a smooth surface. Lower magnification images were obtained using noncontact objective lenses. Higher resolution images used oil-immersion objectives, and in these instances coverslips were temporarily applied to the samples using immersion oil. Initial tests were carried out using the microscope's wavelength (lambda) scan function that produces a signal intensity plot for each excitation wavelength over a range of detected wavelengths for each laser excitation wavelength used. These plots were used to optimize the choice of the excitation laser and to determine the detector window settings used for each channel. The plots also assisted in determining the optimum settings for autofluorescence and for reflection mode, and the two laser excitation wavelengths and detector windows were set to minimize interference.

A 488-nm argon laser was chosen for excitation of fluorescence with a detector window set for fluorescein isothiocyanate–type emission (515–545 nm). A 633-nm helium-neon laser was used with a detector window set at 625–641 nm to detect reflection from the crystalline shell structure at the same spatial position.

Chemical Analyses

Quantitative chemical analysis and element mapping were undertaken using wavelength-dispersive microprobes at the Electron Microscopy and Mineral Analysis Division in the Mineralogy Department, NHM, London. A Cameca SX 50 microprobe was used for spot analyses (15 kV, 20 nA, and 20 μm defocused spot size), and a Cameca SX100 for element mapping (15 kV, 40 nA).

Electron Backscattered Diffraction

Electron backscattered diffraction (EBSD) was carried out in the Department of Geographical & Earth Sciences at Glasgow University using a FEI Quanta 200F field-emission environmental scanning electron microscope in high vacuum mode with an aperture and spot size of 4. The stage is tilted 70°, and the electron beam diffracted by interaction with crystal planes in the shell sample. The diffracted beam interacts with a phosphor screen producing a series of Kikuchi bands that enable crystal identification and orientation to be determined. Data are filtered to remove all data points below a confidence index of 0.1 and the filtered data analyzed using the OIM software from EDAX.

Fourier Transform Infrared Spectrometry

All spectra were recorded at 4 cm^{-1} resolution with 64 scans with a strong Norton-Beer apodization on a Perkin-Elmer Model 1600 Fourier transform infrared spectrometer (FTIR) in the wave number range of 4000 to 450 cm^{-1}. The spectrometer was equipped with a diffuse reflectance accessory that permits DRIFT measurements with high sensitivity on powders. All spectra were corrected by the Kubelka-Munk function. The system was purged and permanently maintained under nitrogen to reduce atmospheric CO_2 and H_2O absorption. A background spectrum was measured for pure KBr. Sample spectra were automatically ratioed against background to minimize CO_2 and H_2O bands. Several spectra from the same samples were measured, and correlation coefficients higher than 95% achieved.

Micro-X-Ray Absorption near Edge Structure Spectroscopy

This work was carried out at the ID21 beamline of the European Synchrotron Radiation Facility. The ID21 Scanning X-ray Microscope uses Fresnel zone plates as focusing optics to generate a submicron X-ray probe, which is used to investigate the sample with various contrast mechanisms

(fluorescence, transmission, phase contrast). An energy-dispersive high-purity Ge detector (Princeton, Gamma-Tech) mounted in the horizontal plane perpendicular to the beam collects the fluorescence emission photons. This geometry minimizes the contribution of elastic scattering. Provided the sample is thin enough, a Si photodiode can also be mounted downstream from the sample to exploit the transmission signal. An energy range between 2 and 7 keV is available, which gives access to the sulfur K-edge at 2472 eV (sulfur in amino acids) and 2482.5 eV (sulfated sulfur in polysaccharides). The X-ray absorption near edge structure spectroscopy (XANES) energy scan around the sulfur K-edge is achieved using a fixed-exit double-crystal Si (111) monochromator located upstream from the microscope, which offers the necessary energy resolution. This experiment required the X-ray microscope to be operated under vacuum to avoid the strong absorption of the sulfur emission lines by air.

Samples were cut perpendicular to the shell surfaces. They were embedded in resin and polished using various grades of diamond paste. The oil residue from the diamond paste was removed with a detergent diluted in hot water for 1 min, then rinsed with tap water. Then samples were etched with 1% v/v acetic acid for 5 s. Because fluorescence emission was used as a contrast mechanism, it was essential that the sample offered a flat surface to the X-ray beam in order to avoid signal fluctuations that could have been produced by sample topography. Additionally, etching of the sample after polishing helped to eliminate potential surface contamination and remains of the diamond pastes and oil.

Scanning Electron Microscope

Microstructural patterns were obtained using a Philips XL30 scanning electron microscope (SEM) at Orsay IDES. Samples were gold coated after light etching using a 1 per mil solution of formic acid with 5% glutaraldehyde added solution (etching time of 40 s).

Results

The variation in the initial activity within the pearl-sac can clearly be observed in natural light. The typically dark to black external color of the Polynesian pearls contrasts with the lighter color of the basal pearl layer. When the nacreous layer seems to be in close contact to the nucleus (Fig. 2a,b), this basal layer is only a few microns thick. In other examples this layer can comprise up to half the total thickness of the pearl-sac (Fig. 2e). Thickness of this initial layer can also vary within a given pearl, leading to formation of irregular protuberances leading eventually to the production of "baroque" pearls (Figs. 1e–h and 2f, arrows).

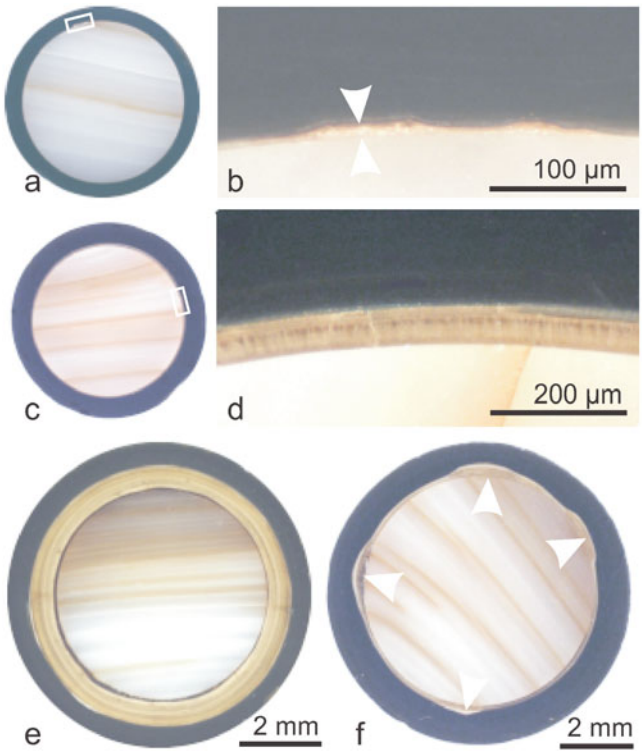

Figure 2. Variability of thickness and irregularity in early mineralization of the pearl layer, observed in natural light. Production of nacreous material correlates to the black color.

Formation of these nonnacreous basal layers is, generally, a temporary process, as the pearl-sac mineralizing activity transforms to production of true pearly nacreous material, the color of which is the characteristic feature of Polynesian pearls.

Fluorescing Properties of the Basal Pearl Layer

When subjected to UV or blue light, the basal pearl layer produces an intense coloration of the emitted light. The overlying nacreous layer itself has a much reduced response to UV or blue light, with the early secretions of the pearl-sac fluorescing strongly blue and blue-green lights (Fig. 3). These images emphasize the diversity of the structures between the nucleus and the nacreous material. Within a basal layer with regular thickness (i.e., Fig. 3a–c), compositional heterogeneity becomes visible through the fluorescence responses with at least two different components present.

Compositional changes between the superimposed layers are also visible through their differences in intensity of emitted light (Fig. 3d–g and h–i). The most remarkable pattern, frequently observed but with numerous variations in detail, is a radial organization of the basal layer. Perpendicular to the nucleus surface, these substructures are also marked by isochronous compositional changes, showing

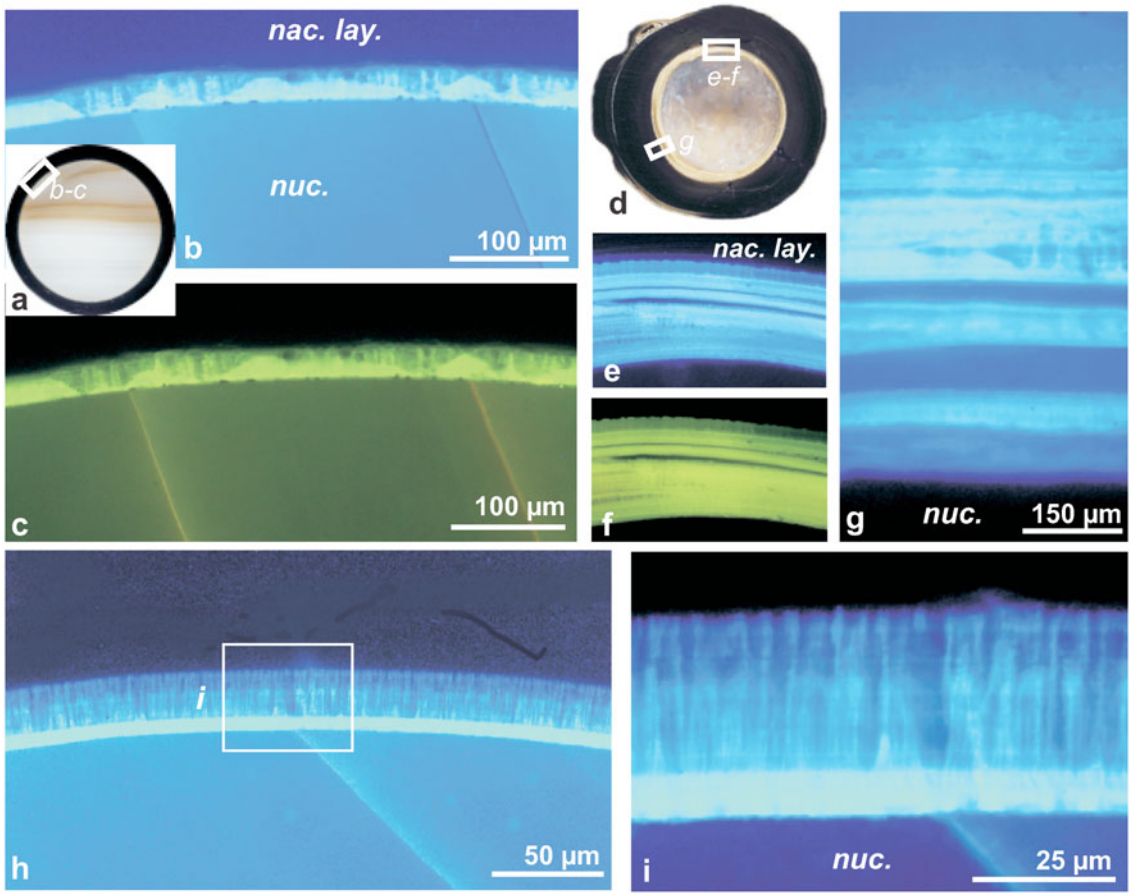

Figure 3. Examples of UV and blue fluorescence of the basal pearl layer (blue and green images, respectively). **a–c:** Within the basal layer (of approximately 30 μm in thickness) differences in fluorescence of the associated structures can be observed. **d–g:** Recovery of the mineralization mechanisms may require several attempts, leading to superimposed layers of fluorescent materials. **h, i:** The most striking feature is the development of radially oriented structures, perpendicular to the nucleus surface. Note the concentric variations in fluorescence, indicating a coordinated cyclic secretory process within the pearl-sac epithelium.

that, in spite of structural heterogeneity, the building material is produced through a cyclical activity of the pearl-sac epithelium.

Diversity of Microstructural Patterns within the Basal Part of the Pearl Layers

Not only is the thickness of the basal pearl layers variable, but the structures developed during this period by the pearl-sac epithelium are also variable from one pearl to another, and sometimes within a given pearl. SEM observations of etched surfaces revealed that two distinct components are always present within the basal pearl layer. Secondary electron images (Fig. 4a–c) that correspond to the fluorescence images (Fig. 3a–c) reveal the presence of a homogeneous and etching resistant material that forms very irregular topographical features. Between these elevated features, a well-defined layered material is deposited (Fig. 4b, arrows).

The columnar, radially-oriented arrangement of the resistant material is frequently more regular (Fig. 4d,e). These secondary electron images correspond to the fluorescent structures seen in Fig. 3h,i. In the highly fluorescing basal layer, the density of the homogenous material is maximal (practically continuous against the nucleus surface). In the main part of the basal pearl layer, this material produces the columnar structures that separate the layered material into distinct sectors. It is worth noticing that in spite of these interruptions a perfect continuity of layering is maintained between the superimposed layers that are less than 1 μm thick.

A contrasting arrangement is shown in Fig. 4f–k. Although this pearl has a relatively normal external appearance (with the exception of some minor defects), the initial development has produced very unusual structures. The regular layering associated with the radial columnar structures, i.e., the most commonly developed structure, is replaced by the formation of weakly fluorescing irregular

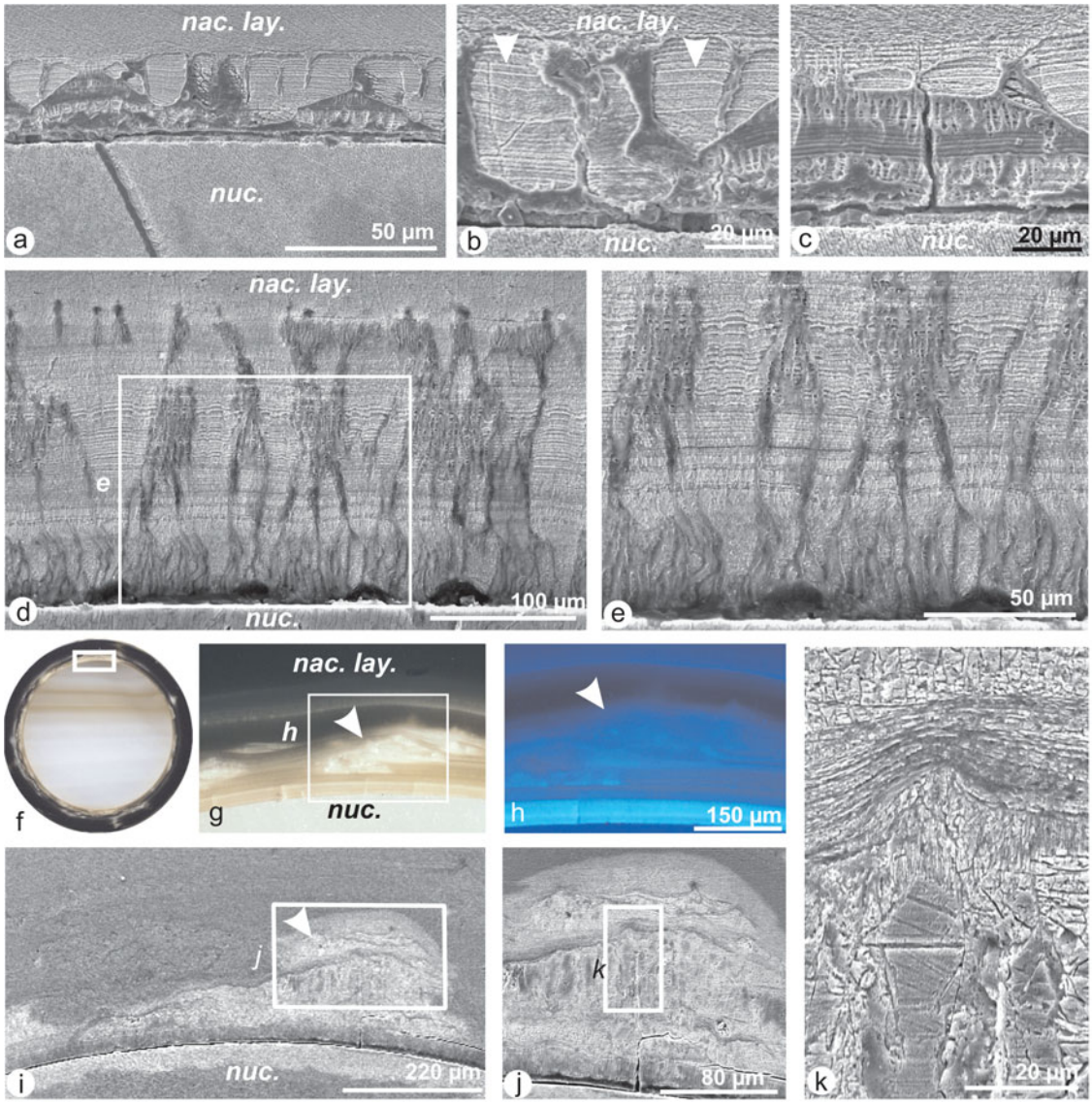

Figure 4. Microstructural diversity of the basal pearl layers. **a–c:** Etching resistant compounds create variously arranged accumulations, the cavities of which are filled by a well-defined layered material. **d,e:** Radially oriented structures frequently occur, producing a complex network of vertical envelopes. When developed further, this process leads to formation of perfect prismatic structures (compare to Fig. 3h,i). **f–k:** In contrast, lack of etching resistant material results in a much less organized microstructure.

amounts of material (Fig. 4g–i, arrows). Secondary electron images (Fig. 4i–k) show a weakly organized structure, sometimes partly layered, but in most cases irregularly fragmented and rather similar to the purely mineral material (Fig. 4k).

Evidence of Prismatic Structures in the Basal Pearl Layer

Among the various radially oriented structures constructed by the pearl-sac epithelium during its early mineralization period, some exhibit a remarkable regularity. Figure 5a–f exemplifies these regular microstructures that are first characterized by their well-defined boundaries. After the highly fluorescent basal episode (Fig. 5b,c), a regular arrangement of high- and low-fluorescing domains can be seen, with the weakly UV fluorescent material corresponding to the etching resistant structures (Fig. 5d,e). This regular array represents a perfect synchronization in layer deposition from sector to sector. Another type of radial structure was also observed (Fig. 5g), in which the layering is even better developed (Fig. 5h). Here, the shape and form of the structures are thinner with a well-developed subparallel array of

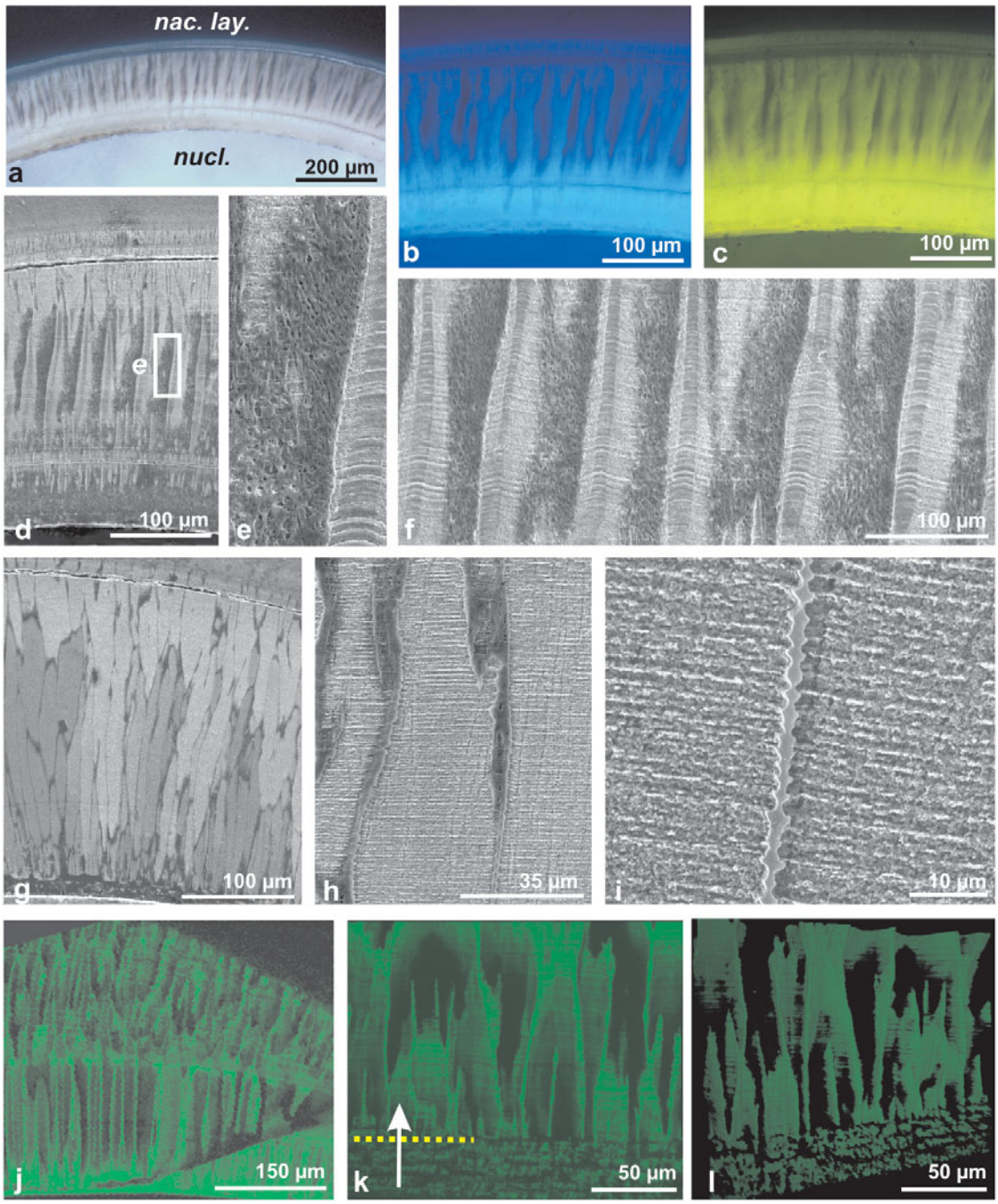

Figure 5. Morphological and microstructural characterization of the prisms. **a–g**, **h–j:** Illustrate the two types of prisms produced when regular envelopes are produced. In both cases, the layering of the mineral phase is visible, but a clear difference exists in its fine scale organization between the two types of prisms. **k–m:** Confocal microscopy images (at 488 nm) show the layered growth of the envelopes as being parallel to the layering of the mineral phase (see also Fig. 5j).

lamellae (Fig. 5i,j) that has a three-dimensional configuration best seen in the fluorescent images (Fig. 5j–l).

The confocal microscopy images (Fig. 5k—compare to Fig. 5i) emphasize the stepping growth mode of the envelopes, as well as the remarkable change that occurs in the behavior of the material that constructed these envelopes. In the early step of secretion (below the yellow dotted line of Fig. 5k), this fluorescing material formed as essentially horizontal layers. However, above this line, the stepping secretory process led to the formation of polygonal enve-

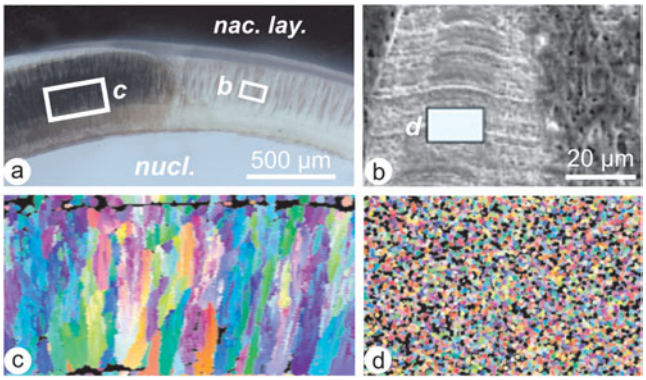

Figure 6. Overall crystallographic patterns of the mineral phases in the prismatic structures of the basal pearl layers. **a,b:** positions of the two EBSD mapped surfaces. **c,d:** Reconstructions of crystallographic orientation of mineral material within the microstructural units. A strong contrast exists between the large, subparallel orientated calcite prisms (**c**) and the small, randomly-orientated aragonite crystals (**d**).

lopes. Thus, the truly prismatic organization of these parts of the basal pearl layer (Fig. 5j) has been recognized by means of the confocal microscopy.

Physical Characterizations of the Mineral Component of the Prisms

In some cases, these two types of prisms have been produced simultaneously during the early developmental stages of a given pearl layer (Fig. 6). Crystallographic information on the two prism types, obtained from EBSD patterns, illustrates that both prism types are indeed crystalline, but that differences exist in their crystal sizes, crystallographic orientations, and crystal structures. Area c in Figure 6a has well-developed, large *calcite* crystals aligned parallel to each other, and normal to the nucleus interface (Fig. 6c). Area b in Figure 6a is composed of small randomly orientated *aragonite* crystals (Fig. 6d). These results illustrate that, within a given pearl, two adjacent sectors of the basal layer can be mineralogically and microstructurally distinct, although they have been produced simultaneously.

Electron Microprobe Characterization of the Prismatic Structures: Element Mapping and Quantitative Analyses

Another example of the simultaneous occurrence of aragonite and calcite in the basal part of a pearl layer is shown in Figure 7a. The calcite prisms (labeled "calc" in Fig. 7a) are clearly delineated from the aragonite region (labeled "arag" in Fig. 7a), where these prisms are less distinct than the calcite prisms. Electron microprobe element distribution maps (Fig. 7c–f) illustrate compositional differences between the calcite and aragonite prisms. The Mg map (Fig. 7c) emphasizes the regular layered growth of the calcitic prisms—

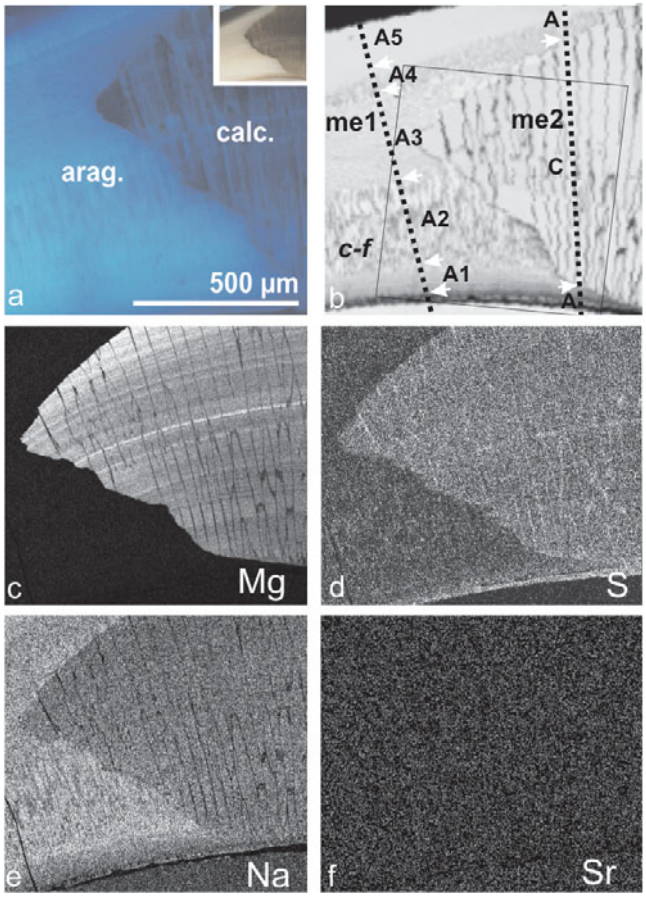

Figure 7. Distribution of minor elements in adjacent calcite and aragonite sectors from a basal pearl layer (CAMECA SX100). **a:** Natural (inset) and UV fluorescence images of the adjacent sectors. **b:** Locations of line profiles (me1 and me2) for quantitative analyses (see CAMECA SX50 results in Figs. 8 and 9). **c–f:** Element distribution maps for Mg, S, Na, and Sr. Mg (**c**) is higher in the calcitic part; S (**d**) is also higher in calcite (compare to sulfated polysaccharide distribution below); Na (**e**) is higher in the aragonitic areas (typical for Ca-biocarbonate mollusks); the Sr distribution (**f**) reflects the relatively low content of this element in aragonitic mollusks, in contrast to other aragonitic skeletons such as fibers of Scleractinian corals.

the concentration of Mg varies within different growth zones and cross-cutting individual calcite prisms. Maps for S and Na do not show such strong concentration variations but are inversely related in that calcite is enriched in S and depleted in Na, relative to aragonite. Sr is uniformly low in both calcite and aragonite.

Quantitative Electron Microprobe Analyses of Calcite and Aragonite Prisms

Quantitative information for some minor elements (Na, Mg, S, Sr) was obtained through a series of spot measurements carried out using the CAMECA SX50 electron micro-

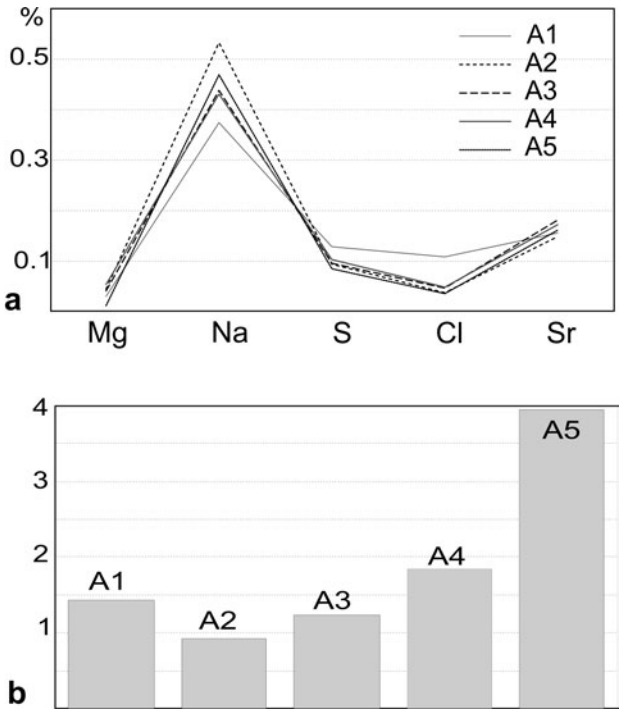

Figure 8. **a:** Five distinct compositional zones can be recognized within the aragonite (see Fig. 7b for locations of each zone). Changes in pearl-sac metabolism are assessed by variation of minor element concentrations in aragonite from the most internal layer (A1) to external (A5). **b:** L ratios emphasize the difference between successive aragonite layers A1 to A5.

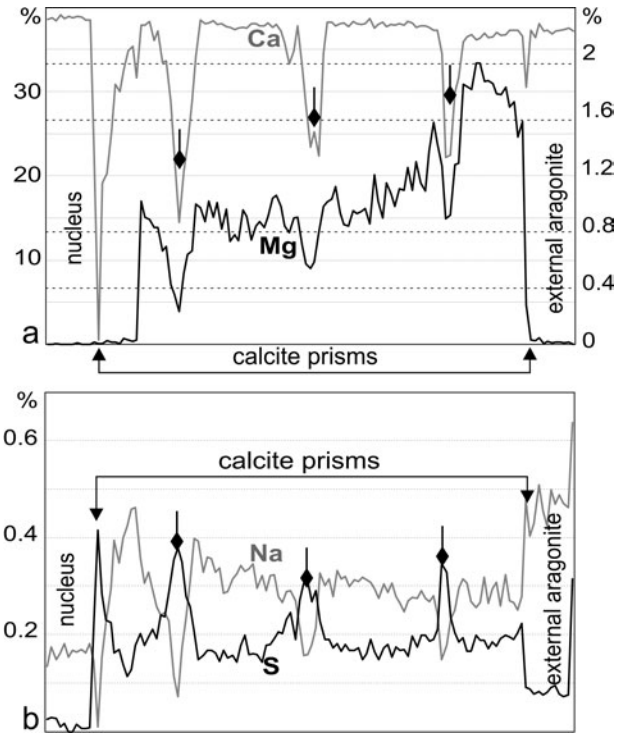

Figure 9. Elemental variations within the calcite prisms (me2 transect, Fig. 7). **a:** Profiles for Ca and Mg. The Ca concentration in calcite is relatively constant (with the exception of three "spikes" that represent regions of prism membranes). In contrast, Mg increases across the length of the profile and has also an oscillatory distribution corresponding to the Mg map of Fig. 7c. **b:** Profiles for Na and S. There is broadly an inverse relationship between these elements, with the prism membranes relatively enriched in S.

probe. Two line profiles were made in the same area (Fig. 7b: me1 and me2).

The first profile (me1) cuts across several distinct aragonitic structures from the nucleus to the nacreous layer of the pearl (Fig. 8).

The ratios Sr^{2+} and Mg^{2+} to Ca^{2+} (or L ratios, Loreau, 1982) are also indicative of the aragonitic composition of the layers A1–A5 (Fig. 8). These ratios are in accordance with those calculated from published data (Milliman, 1974). Average L values in bivalve shells = 1.5 ± 1.0 (Loreau, 1982) for layers A1–A4, but the value for layer A5 is relatively high.

The majority of the second line (me2) passes through the large calcite prisms. The Ca profile in me2 clearly shows the low concentrations of this element in the organic layer between the nucleus and the first pearl layers (Fig. 9a, left). Within the calcite prisms, the Ca concentration is relatively constant (it decreases when beam is focused on the prism envelopes). In contrast, the Mg concentration slowly increases from the beginning to the upper part of the prisms and has an oscillatory distribution throughout the profile. The end position of this profile is on aragonite.

In the calcite prisms, the concentration of Mg reaches 1.138 wt%. This high value contrasts with typically 0.25 to 0.44 wt% in the various aragonitic structures (Fig. 8). Na and Sr concentrations are low in the calcite prisms, whereas S concentrations are low in the aragonite layers.

IR Absorption and XANES Mapping of the Organic Components in the Prisms

The infrared spectra of the calcite and aragonite are characterized by three major bands attributed to the carbonate radical CO_3^{2-}: $\nu 3$ at 1429 cm^{-1}, the $\nu 2$ doublet 877–848 cm^{-1}, $\nu 1$ between 1060 and 1087 cm^{-1}, and $\nu 4$ at 713 cm^{-1} for the calcite group; $\nu 3$ at 1471 cm^{-1}, $\nu 1$ between 1073 and 1085 cm^{-1}, and two doublets: $\nu 2$ at 858–844 cm^{-1} and $\nu 4$ at 713–700 cm^{-1} for the aragonite group.

The aragonite spectrum of the pearl has the main features typical for aragonite (Table 1, Fig. 10). However, the first part of the $\nu 2$ doublet is absent. Some amide bands (A, I, and II) are present, indicative of the presence of proteins and/or sugars. The pearl calcite spectrum shows the main features of the mineral calcite, despite the absence of the second part of the $\nu 2$ doublet (Table 1, Fig. 10). Numerous amide I and II bands are present, showing the complexity of

Table 1. Numerical Values of IR Absorption Bands in Purely Mineral Aragonite and Calcite Compared to Aragonite and Calcite Prisms of the Basal Pearl Layer (Pearl).

	ν1	ν2	ν3	ν4	Amide A	Amide I	Amide II	COOH
Aragonite	1085	860877	1493	700712				
			1429					
Pearl	1082	859	1472	700713	3292	1670	1556	
			1457		3266	1654		
						1646		
Calcite	1087	848877	1435	713				
	1060		1407					
Pearl	1084	876	1455	713	3297	1683	1574	1734
			1446			1674	1558	
			1434			1668	1538	
			1428			1661	1531	
			1424			1652	1518	
						1646	1515	
						1635		
						1616		

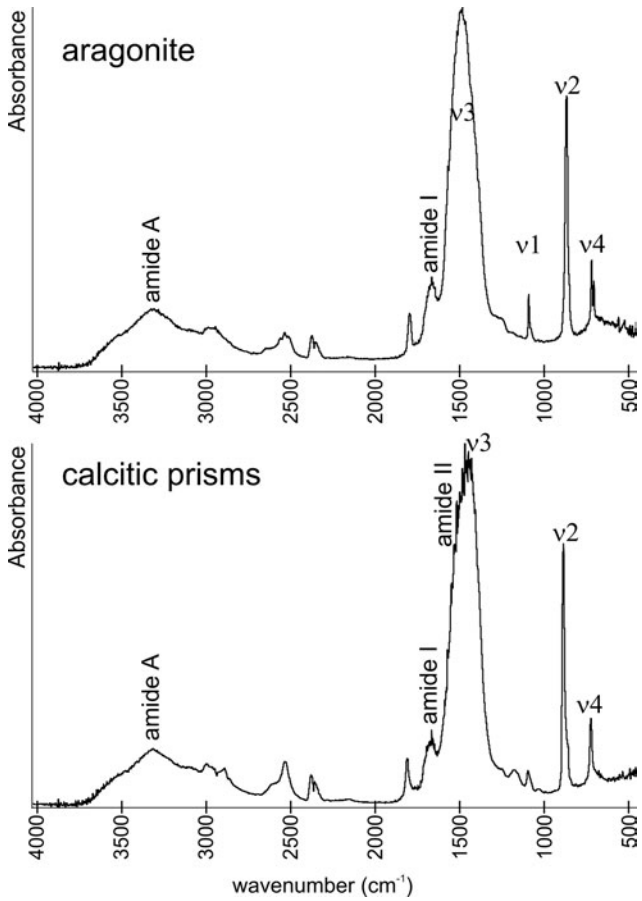

Figure 10. Infrared spectrum showing the organo-mineral composition of the aragonite and calcite extracted from pearl.

the organic matrices. Of note is that the intensities of amide II bands are higher than those of amide I, an unusual feature.

Two ratios have been calculated from FTIR spectra to estimate the organic/mineral ratio. For aragonite, the first ratio is based on the absorbance intensities of the amide A band divided by the 860 cm^{-1} part of the ν2 band: amide A/860. The second ratio is based on the absorbance intensities of the stronger amide I band divided by the 860 cm^{-1} part of the ν2 band: amide I/860. For calcite, the 878 cm^{-1} band is used. In such ratios, all the organic matrices (soluble and insoluble) are included. In aragonite, the A/860 ratio = 0.22 and the I/860 ratio = 0.34: in calcite these values are equal to 0.22 and 0.29, respectively.

XANES Mapping Illustrating the Correlation between the Biochemical Changes and Mineralization

The overall variations in secretion of the pearl-sac during the early mineralization period, as well as the localized differences in each of the successive layers, can be established by XANES mapping using synchrotron radiation. By resolving the organic sulfated sulfur peak at 2.4825 keV from the amino acids sulfur peak at 2.472 keV, the distribution of polysaccharides and proteins can be observed. In the prismatic structures of the basal pearl layer, a precise correlation can be seen between the mineralized areas (aragonite) and the higher concentrations of polysaccharides (Fig. 11a,b). Additionally, the distribution of proteins (through the sulfur in cysteine and methionine) is seen

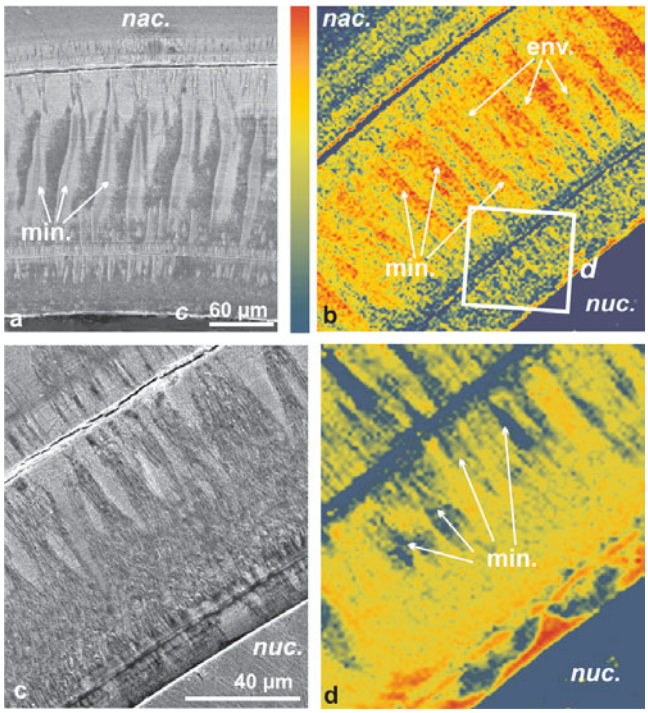

Figure 11. XANES maps from synchrotron radiation of a basal pearl layer. **a,b:** Map obtained at 2.4825 keV reveals a predominance of the sulfated polysaccharides in the mineralized areas (the color palette represents qualitative information). **c,d:** Distribution of proteins through mapping of the sulfur at 2.472 keV (same color palette). Note the irregular distribution of proteins in the basal layer, in contact with the nucleus surface. **a** and **c** are secondary electron images.

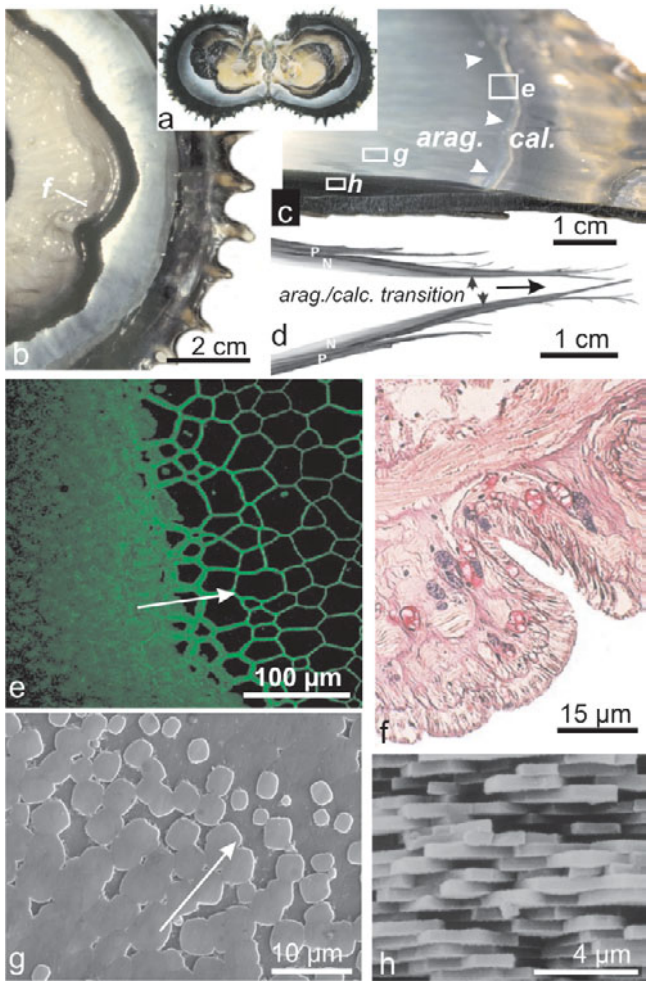

Figure 12. Main structural patterns of the shell of the pearl oyster *Pinctada margaritifera*. **a,b:** Mantle and shell of a *Pinctada* (internal side of a valve). **c,d:** View of a sectioned valve showing the limit between calcite and aragonite deposition (arrows) and the continuous overgrowth of prisms by the nacreous layer. **e:** Confocal microscope image of the internal surface of the shell at the limit between prismatic layer (right side) and nacreous (left). Nacre spreads (arrows) onto the internal surface of the prisms (the growth of which then stops). Compare to **c** and **d**. **f:** Histological section of the mineralizing epithelium (outer layer of the mantle) (courtesy F. Blanc). **g,h:** Secondary electron images of the nacreous tablets: **g**, flattened round-shaped to polygonal units; **h**, approximately 0.5 μm thick.

to be predominantly in the prism envelopes (Fig. 11c,d: yellow to red colors), compared with the mineralized areas (green).

Discussion

The *Pinctada margaritifera*, the Pelecypod species from which pearls are produced in Polynesia, is known as the "black lip pearl oyster" because of the black pigmented material that forms the outer layer of the shell valves (Fig. 12a,b). This material consists of calcite deposited at the edge of the mantle, whereas the central part of the same organ produces the "mother of pearl," composed of aragonite. Calcite and aragonite, the two main structural forms (polymorphs) of calcium carbonate, are thus produced simultaneously by the external layer of the mantle, but in strictly separated areas. On the internal side of the shell, the line that separates the calcitic and aragonitic areas is clearly visible (Fig. 12c, arrows), making evident the biological control on mineral deposition. As a consequence of shell growth, the aragonitic layer covers the internal side of the calcitic outer layer during life (Fig. 12d, arrows).

Summary of Morphological and Compositional Patterns of the Calcitic and Aragonitic Units of the *Pinctada* Shell

The precision of the biological control on shell mineralization is still more obvious when considering the morphology and spatial arrangement of the mineral units that compose

the two shell layers. The calcite is deposited as prisms, elongated units the lengths of which are perpendicular to the shell surface. The polygonal sections of these prisms are thus clearly visible at the internal surface of the outer shell layer (Fig. 12e, right side). From a microstructural viewpoint, the prisms are large units, with a mean transversal section of about 50 μm and may reach a maximum length of up to 3 to 4 mm in adult shells. It is noteworthy that no relationship can be found between the sizes of the prisms and the dimensions of the mantle layer cells by which the prisms are produced (Fig. 12f). The processes by which prism dimensions are fixed, and crystallization controlled take place extracellularly.

In contrast to the calcitic prisms, aragonite is deposited as small flattened units approximately 6–8 μm in transversal dimensions and 0.5–0.7 μm in thickness (Fig. 12g,h). It has long been observed that neither calcite nor aragonite exhibit the growth mode typical for their inorganic mineralogy. Biogenic nacreous tablets, for instance, are flattened on their crystallographic *c* axis, which is normally the axis of maximum growth rate for inorganic aragonite.

Confocal microscopy emphasizes the major patterns of these two microstructural units: both are deposited under strict control of organic components secreted by the cells of the external layer of the mantle (Jabbour-Zahab et al., 1992). The most visible of these organic compounds are the envelopes of the microstructural units. On the right side of Figure 12e, the prism envelopes are transversally sectioned because the prisms are growing inward, perpendicular to the shell surface. On the left side, the apparently continuous green surface results from laser-induced fluorescence of the organic envelopes of the nacreous tablets.

It is worth remembering that when the graft was cut from the nacreous-producing area of the *Pinctada* mantle, it was producing these precisely controlled aragonitic tablets, undoubtedly the most studied of all biominerals. It is important to emphasize how different are the structures produced by the pearl-sac, 1 month after the grafting process.

The Early Mineralization of the Pearl-Sac Compared to Morphological, Mineralogical, and Biochemical Patterns of the Nacreous Units

Our observations on the structures produced by the pearl-sac epithelium in its early mineralizing phases illustrate that there is a complex and subtle mix of morphological, mineralogical, and biochemical features.

The most striking observation is the frequency of radially oriented units (perpendicular to the nucleus surface), in contrast to the thin horizontal layering of the nacreous aragonite. It is clear that the cyclical secretory metabolism of the mantle has persisted in the pearl-sac, as shown by the layering visible in the basal layer of any pearl (with some rare and localized exceptions, see Fig. 4i–k). However, the secreted organic material shows a persistent trend to create the radially oriented features that may result in perfect prismatic structures. In this respect, these observations support Kawakami's interpretation of a "regeneration" of the mantle during pearl-sac formation.

But most surprisingly, the mineral component of the prisms can be constructed of either aragonite or calcite materials. Although not described from a microstructural viewpoint, aragonite in the basal pearl layer was recently detected (Ma et al., 2007), raising a question about Kawakami's theory (1952) of a normal microstructural sequence produced by the pearl-sac epithelium. In fact, with respect to the biomineralization mechanisms (see Weiner & Dove, 2003 for review), production of aragonitic prisms by an epithelium derived from a *Pinctada* mantle is an example of microstructural chimera. The formation of aragonite prisms requires simultaneous production of two sets of organic compounds normally separated in the *Pinctada* mantle. One set of these organic molecules must be able to develop an extracellular self-assembly process leading to the formation of the radially oriented envelopes (perpendicular to the substrate). The other part of the mineralizing matrix secreted by the pearl-sac epithelium enables aragonite precipitation. Such a blend of organic molecules does not exist in the shell of *Pinctada*. As a rule, the organic compounds that lead to the formation of the prismatic envelopes are associated with molecules that produce calcite; whereas aragonite normally occurs only within the horizontally flattened envelopes of the nacreous tablets.

In support of the "microstructural chimera" interpretation, the sectors that show the simultaneous occurrence of calcitic and aragonitic prisms, in close contact but clearly separated, are synchronous with respect to the layering (Fig. 13). Clearly in such cases, the corresponding areas of the pearl-sac epithelium were made of adjacent domains with distinct secretory metabolisms.

Modification of Genomic Activity during the Pearl-Sac Formation

The abnormal, irregular, and sometimes quite aberrant microstructural organization (the aragonite prisms) described above in the basal pearl-layer leads to admit the occurrence of unusual associations of mineralizing organic matrices. But we can observe that all the material products (organic and mineral) involved in these early-mineralization processes can be recognized as belonging to the basic *Pinctada* metabolism. Within these abnormal microstructures produced in the basal pearl layers, the chemical compositions of calcite and aragonite (whatever their microstructural arrangements) are quite comparable to either regular calcite of the prisms or the aragonite of the nacre. Organic materials, such as sulfated polysaccharides predominant in the normal calcitic prisms, or protein components exhibit comparable overall compositions.

This suggests that the grafting operation and the subsequent peal-sac formation process have led to disturbance in the genomic activity of the cells, resulting in the various

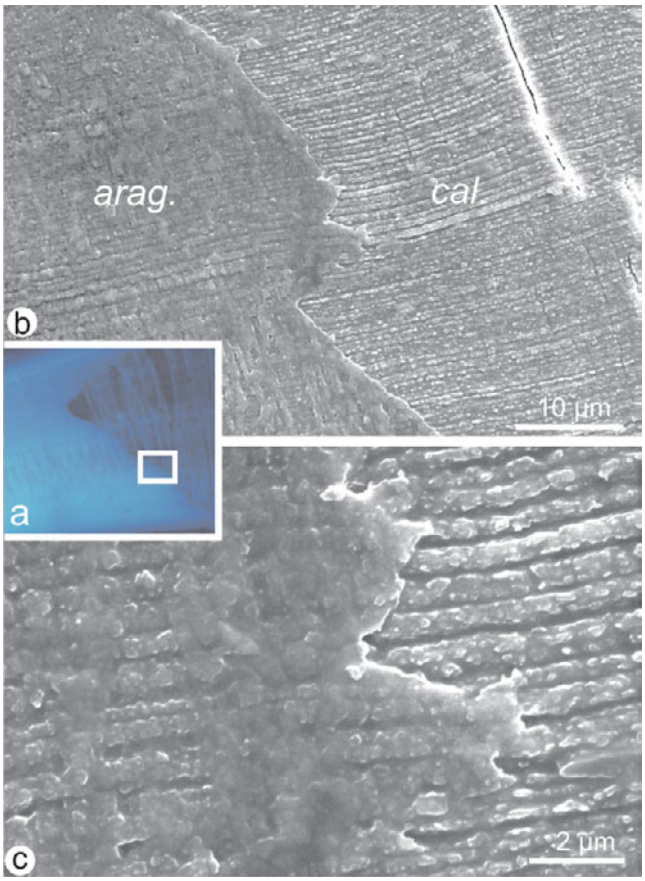

Figure 13. Example of synchronous calcite/aragonite layering within the prismatic structures of the basal part of pearl layer. Between these two adjacent areas, the differences in crystallization produce two distinct domains within the pearl-sac epithelium at this early developmental stage.

and very unusual molecular associations found in the structures from the early mineralizing period. A recent study (Takeuchi & Endo, 2006) on the coordinated expression of genes encoding for major shell matrix proteins clearly indicates that regular separation of calcite and aragonite secretory activity, as it occurs in normal shells, is due to strict control exerted at the scale of the whole animal. In contrast, the abnormal organo-mineral associations observed in the basal pearl layer can be interpreted as a consequence of the uncontrolled mineralization process in the early stages of pearl-sac formation. Remarkably, a recovery process generally occurs. Among the 30 studied pearls, only 3 have shown very uncommon growth patterns, leading to permanent production of the calcite prisms (the black or brown pigmented zones visible on Fig. 1e–h).

With respect to pearl quality control and the sustainable development of the pearl industry, the degree to which this recovery process enables a new production of regular nacreous material is an important question. We can reasonably hypothesize that the grafting sequence plays a key role in influencing further activity of the pearl-sac. Therefore, from a practical viewpoint, in-depth analysis of the pearl-sac early mineralization may help to improve the technical approach during the two key steps of the grafting process, with direct consequences on the quality and regularity of the pearl production process itself.

Conclusions

1. In contact with the nucleus, the lower parts of the pearl layer show that postgrafting mineralization by the pearl-sac strongly differs from the regular nacreous material that was produced by the graft, just before it was cut from the animal mantle.
2. A very unusual association of organic and mineral materials is deposited during the early mineralization period, leading to formation of various structures that appear, from their irregularity, to be only weakly controlled. However, a general trend to forming radially oriented structures can be observed. This may result in the formation of prisms, either aragonitic or calcitic, sometimes produced simultaneously in adjacent areas of the pearl-sac.
3. Compared to the overall features of the normal nacreous material in the *Pinctada* shells, these chemical and structural features of the materials produced during the early activity of the pearl-sac suggest that modifications have occurred in genomic activity of the grafted epithelium during pearl-sac formation.

Acknowledgments

This research was supported by a SYNTHESYS grant, the financial support of the French ANR through contract ANR-06-BLAN-0233, a ESRF grant (EC208), and (*pro parte*) by the ESF-EuroCores EuroMinScI *BioCalc* project. The authors are also indebted to J. Spratt, A. Kearsley, and to the members of the preparative team of the NHM Mineralogy Department. A. Pérez-Huerta acknowledges financial support from the BBSRC (BB/E003265/1).

References

Gervis, M.H. & Sims, N.A. (1992). *The Biology and Culture of Pearl Oysters (Bivalvia, Pteriidae)*. Makati, Manilla, Philippines: International Center of Living Aquatic Resources Management.

Jabbour-Zahab, R., Chagot, D., Blanc, F. & Grozel, H. (1992). Mantle histology, histochemistry and ultrastructure of the pearl oyster *Pinctada margaritifera*. *Aquat Liv Res* **5**, 285–297.

Kawakami, I.K. (1952). Mantle regeneration in pearl oyster (*Pinctada martensii*). *J Fuji Pearl Inst* **2**, 1–4.

Loreau, J.P. (1982). Sédiments aragonitiques et leur genèse. *Mém Mus ntnl hist nat N.S.* **C47**, 1–312.

Ma, H., Zhang, B., Lee, I.S., Quin, Z., Tong, Z. & Qui, S. (2007). Aragonite observed in the prismatic layer of the seawater-cultured pearls. *Front Mat Sci China* **1**, 326–329; DOI 10.1007/s11706-007-0061-6.

Milliman, J.D. (1974). *Marine Carbonates*. New York, Heidelberg, Berlin: Springer Verlag.

Takeuchi, T. & Endo, K. (2006). Biphasic and dually coordinated expression of the genes encoding major shell matrix proteins in the pearl oyster *Pinctada fucata*. *Mar Biotech* **8**, 52–61.

Weiner, S. & Dove, P.M. (2003). An overview of biomineralization processes and the problem of the vital effect. In *Biomineralization*, Dove, P.M., De Yoreo, J.J. & Weiner, S. (Eds.), **S54**, pp. 1–29.